Article

The Effect of Refined Coherent Grain Boundaries on High-Temperature Oxidation Behavior of TiAl-Based Alloys through Cyclic Heat Treatment

Keren Zhang *, Lele Zhang and Jinguang Li

School of Materials Science and Engineering, Xi'an Shiyou University, Xi'an 710065, China
* Correspondence: zkrnwpu@163.com

Abstract: The grain size of the full lamellae TiAl-based alloy changes from ~400 μm to ~40 μm through the precipitation of metastable structures by cyclic heat treatment. Based on this, two kinds of variant selection processes—coherent metastable γ variants precipitated during the air-cooling process and α_s variants precipitated during the holding at a single α phase region process—are identified to promote the formation of refined Type I and Type II coherent grain boundaries. The oxidation tests at 1000 °C for 100 h show that the formation of refined coherent grain boundaries can greatly improve oxidation resistance by inducing the continuous multi-layer protective barrier consisting of (Ti, (Nb, Ta))O_2, TiN, and Al(Nb,Ta)$_2$. This protective barrier inhibits the inward diffusion of oxygen and nitrogen.

Keywords: grain size; oxidation; titanium aluminides; multi-layer barrier; coherent boundaries

1. Introduction

Due to their high specific stiffness, good creep properties, and oxidation resistance at high temperatures, cast TiAl-based alloys with low density (3.8~4.3 g/cm^3) are important for applications in aerospace and automotive engines to improve fuel economy [1–3]. However, the lack of oxidation resistance over 800 °C and the associated embrittlement of γ-TiAl and α_2-Ti$_3$Al intermetallic phases could limit the application of TiAl-based alloys [4]. Although the Al content is relatively high, it is difficult to form a protective continuous Al$_2$O$_3$ oxide film in the outermost layer due to the similar thermodynamic activity of TiO$_2$ and Al$_2$O$_3$ and the faster growth velocity of TiO$_2$. Instead, a TiO$_2$ + Al$_2$O$_3$ mixed layer or TiO$_2$ layer is preferred [5,6]. The intrinsic porous structure of rutile TiO$_2$ and the loose structure of TiO$_2$ + Al$_2$O$_3$ are not helpful in improving the oxidation resistance [7,8].

Therefore, numerous methods have been attempted to improve high-temperature oxidation resistance. For micro-alloying elements added in TiAl-based alloys, the addition of Nb [7], Si [4], Ta [6], Mo [5], and Sn [8] has been found to be beneficial in promoting the formation of a strong and continuous oxide Al$_2$O$_3$ layer or other continuous metal-oxide layer. Besides, changes in microstructure, including grain size, can also affect the oxidation behavior of TiAl alloys [9–12]. The fine full lamellae (FFL) microstructure has been demonstrated to have the best mechanical properties, particularly in terms of tensile ductility at room temperature [13–17]. However, it has been found that the influence of the grain size of the α_2 + γ lamellae colony on the oxidation behavior of a TiAl-based alloy presents both positive and negative effects. On the one hand, the grain refinement can introduce more grain boundaries, which provide channels for oxygen or nitrogen diffusion to the substrate and consequently reduce oxidation resistance [9,10]. On the other hand, an increased number of grain boundaries can also facilitate the movement of Al atoms to form a continuous and strong Al$_2$O$_3$ protective layer on the surface, thereby preventing further diffusion of oxygen or nitrogen [18]. Therefore, it is necessary to clearly illustrate whether grain size has a positive or negative effect on the oxidation behavior of TiAl alloys.

In this study, we investigated the effects of grain size and grain boundary structure on the high-temperature oxidation resistance of a TiAl-based alloy by performing isothermal oxidation tests at 1000 °C for 100 h. Surprisingly, our research presents clear evidence that the FFL TiAl alloy has coherent grain boundaries and much better oxidation resistance than the coarse full lamellae (CFL) TiAl alloy. Moreover, the mechanism of oxidation behavior affected by the coherent grain boundaries was discussed in depth.

2. Materials and Methods

The cast γ-TiAl ingot (Ti-48Al-3Nb-2Ta (at.%)) was melted by a consumable electrode arc melting furnace in an argon atmosphere and repeated three times. Then the ingot was hot isostatically pressed (HIP) at 1280 °C/150 MPa for 4 h, followed by homogenization treatment at 1430 °C (above the single α-phase region) for 2 h. A cyclic heat treatment was conducted. One cycle of heat treatment includes heating to 1430 °C for 5 minutes, then cooling to room temperature in the air. After that, heat to 1280 °C (in the $\alpha + \gamma$ two-phase region) for 4 hours, then cool in the air. After 5 cycles of heat treatment, the samples were heated at 1430 °C for 5 minutes, then cooled in the air for post-processing.

For oxidation tests, 8 mm × 8 mm × 8 mm samples were cut off from the homogenized and cyclic heat treatment samples. Prior to oxidation, samples were mechanically ground by standard SiC papers with different meshes (from 400 to 5000 mesh) to obtain sufficient surface polish. Then, each sample was ultrasonically cleaned in acetone for 20 minutes. To ensure the repeatability and scatter of the experiment, two duplicate specimens of each alloy were measured simultaneously. The high-temperature oxidation tests were performed in a corundum crucible at 1000 °C for 100 h in laboratory air conditioning in a box furnace. The samples were transferred into an oven, with the oven door open at a certain angle to ensure that all surfaces of the samples were in full contact with the air. The weight of each specimen was measured after a particular period (5 h, 15 h, 25 h, 35 h, 50 h, 70 h, and 100 h) using a high-precision (0.001 mg) FA2204B electronic balance (Shandong, China) after being cooled in air for approximately 40 min. Afterward, the crucibles were placed back in the furnace operated at 1000 °C.

The surface phase composition after 100 h of isothermal oxidation was characterized by X-ray diffraction (XRD, D/max-RB) with Cu Kα radiation performed with a 2θ angle of 20° to 90° and a scanning speed of 5°/min. The morphologies of the oxide surface and cross-sectional morphology of the oxide film were observed by SEM using FEI Helios NanoLab G3 (Waltham, MA, USA). It is necessary to ensure that the oxide film in the image is long enough and the oxide film/substrate interface can be clearly seen. The oxide film thicknesses were measured at five different positions at equal intervals. Due to the resolution of EBSD, which is not able to differentiate between the six variants of γ phase, the γ-L1$_0$ structure has a tetragonality symmetry (c/a = 1.02) (which is possible using TEM), and the γ variants were indexed as a faced-centered cubic (fcc) crystal. The HRTEM and HAADF images were carried out on a FEI Themis Z double Cs corrector transmission microscope (Waltham, MA, USA) operating at 300 kV.

3. Results

3.1. Microstructure of CFL and FFL Alloys

The schematics of the cyclic heat-treatment route of the as-cast Ti-48Al-3Nb-2Ta (at.%) alloy are illustrated in Figure 1a. A coarse full lamellae (CFL) microstructure with an average grain size of ~400 μm can be observed after homogenization treatment (Figure 1b). Metastable structures: feathery-like structures and massive γ phase are observed embedding in the lamellae colony with different crystal orientations. Previous studies have shown that [19,20] metastable structures are preferred after heat treatment in a single α-phase region and cooling at a relatively high rate. Furthermore, the cooling rate, which needs to promote the formation of metastable structures, is found to be lowered by the addition of heavy elements such as Nb and Ta [21,22]. Therefore, in this study, the feathery-like structures and massive γ phase can be observed after the air cooling condition of the

Ti-48Al-3Nb-2Ta alloy. Finally, after five cycles of cyclic heat treatment and post-processing, the primary CFL microstructure is completely different from the fine full lamellae (FFL) microstructure (Figure 1c).
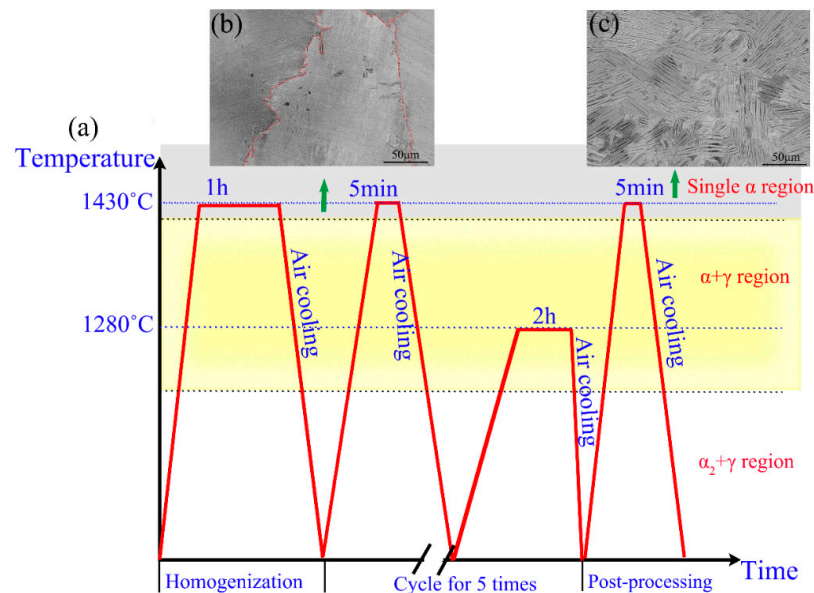

Figure 1. Schematics of cyclic heat-treatment route (**a**) and corresponding microstructure (**b**) after homogenization treatment, (**c**) after five cycles of cyclic heat treatment.

The inverse pole figure (IPF), kernel average misorientation (KAM) maps, grain boundary maps, and misorientation distributions of alloys after cyclic heat treatment with zero, three, and five cycles are shown in Figure 2 to further investigate the characteristics of the refinement of these lamellar colonies. All the samples consist of $\alpha_2 + \gamma$ lamellar colonies. The metastable structure of feathery-like structures and massive γ phase with different grain orientations can be observed when the grain size is large, as shown in Figure 2a,b. After five cyclic heat treatment processes, the coarse microstructure disappears and a fine, fully $\alpha_2 + \gamma$ lamellar microstructure is observed. The grain size was refined from 400 μm to about 40 μm (Figure 2d–f).

Furthermore, during cyclic heat treatment, the structure of the interface also changes, as shown in Figure 2j–l. The lamellar colonies with the following $\Sigma 1$, $\Sigma 3$ coincidence site lattice (CSL) boundaries are observed: It can be found that the volume fraction of $\Sigma 3$ 60°<111> twin-related boundary decreases from 52.8% to 41.6%, and that of $\Sigma 1$ boundary increases from 5.51% to 20.3% after five times cyclic heat treatment. It should be noticed that for CFL alloy, the inner lamellar colony mainly consists of $\Sigma 3$ CSL boundaries, indicating the interfaces between γ/γ lamellae are primarily twin-related interfaces. But the grain boundaries are found to be disordered, large-angle boundaries. For FFL alloy, the majority of grain boundaries are identified as $\Sigma 1$ and $\Sigma 3$ coincidence site lattice boundaries. The misorientations after 0° to 5° for 0, 3, and 5 cycles are illustrated by utilizing the KAM maps shown in Figure 2g–i, where the CFL alloy with a metastable structure presented a higher strain than the FFL alloy due to the longtime heat treatment (Figure 2j–l).
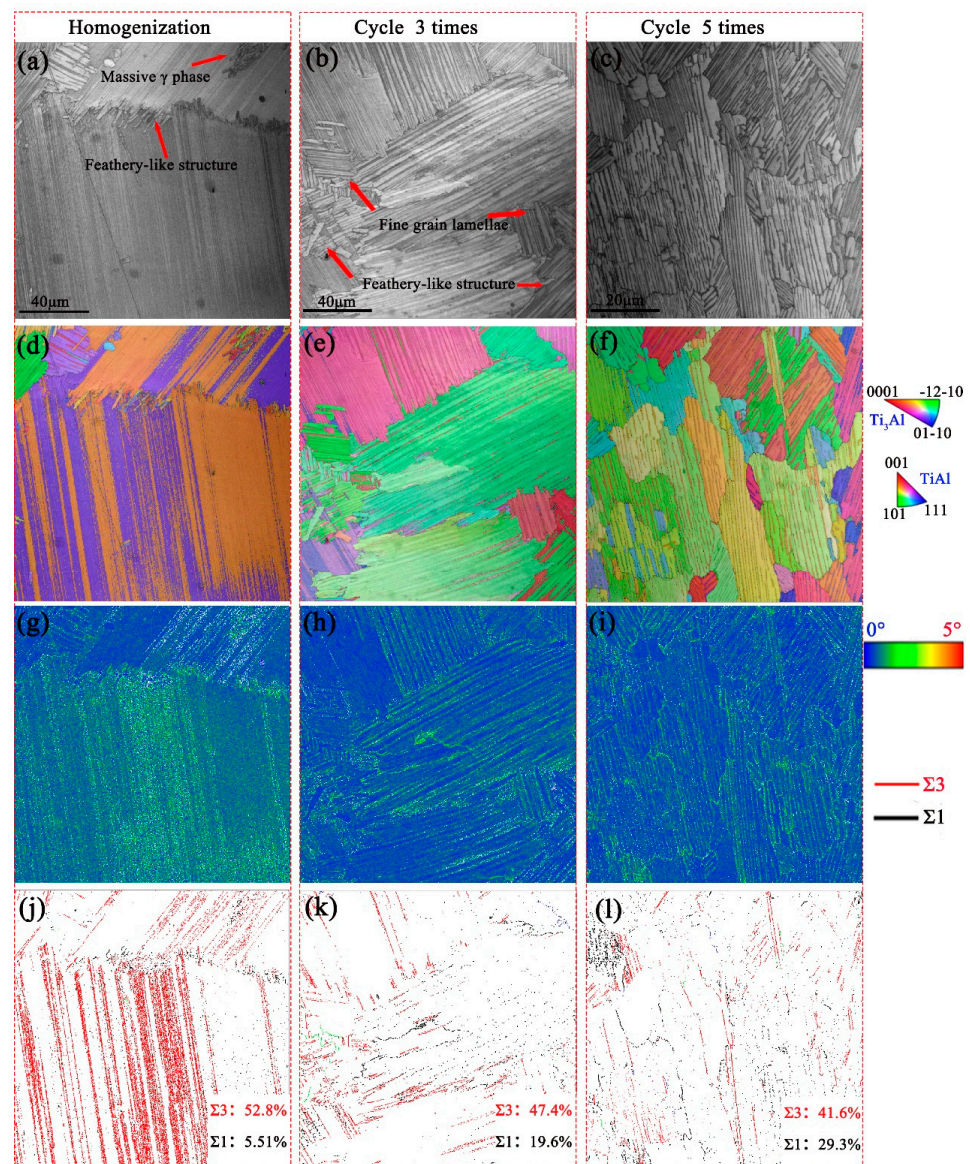
Figure 2. Band contrast, Inverse pole figure (IPF), KAM and boundary maps of the Ti-48Al-3Nb-2Ta alloy with different cycle times; (**a**,**d**,**g**,**j**) after homogenization; (**b**,**e**,**h**,**k**) 3 cycles; (**c**,**f**,**i**,**l**) 5 cycles.

Figure 3 shows the enlargement of the local grain orientation information of the microstructure after five cycles. According to the PFs, the Blackburn orientation relationship of $\{0001\}\alpha_2//\{111\}\gamma$ between α_2 and γ phases can be well-defined. Furthermore, it can be seen that Grain 1 and Grain 2 share the same γ grain that $\{111\}\gamma1$ equal to $\{111\}\gamma2$, but have different α_2 grain, that α_{s1} has 71° misorientation with α_{s2}; for Grain 3 and Grain 4, the orientation of α_2 grain is nearly the same, but $\gamma3$ and $\gamma4$ grain have deviation of 2°, which low-angle grain boundaries may confirm to be 120° rotational interface.
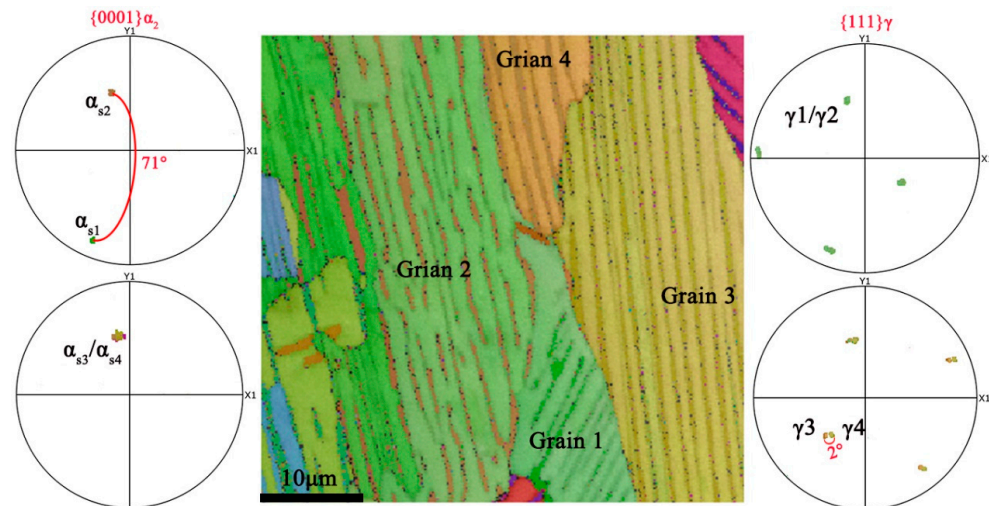
Figure 3. Inverse pole figure (IPF) and pole figures (PFs) maps of Ti-48Al-3Nb-2Ta alloy after cycling five times.

Typical TEM observations were carried out to further characterize the structure of grain boundaries after cycle five times. Two typical grain boundaries are identified using SADPs and HAADF techniques, as shown in Figure 4. From the relationship of $\left[\bar{1}10\right]\gamma1//\left[\bar{1}10\right]$ $\gamma2//\left[11\bar{2}0\right]\alpha_{s1}$ of Type I boundary shown in Figure 4a,c,f, it can be concluded that although the lamellar orientation of Grain 1 and Grain 2 has 71° misorientation, the crystal structure of γ grain in Grain 1 and Grian 2 is totally the same. It is in accordance with the EBSD results of Grain 1 and Grain 2 shown in Figure 3. Furthermore, from the $\left[\bar{1}10\right]\gamma2//\left[101\right]$ $\gamma3//\left[11\bar{2}0\right]\alpha_{s3}$ relationship of Type II boundary shown in Figure 4b,d,e, it can be concluded that the crystal structure of α_s grain in Grain 2 and Grain 3 is identical, while $\gamma2$ and $\gamma3$ show 120° rotational boundaries with 2° misorientation of α_2 lamellae. It is also certified by the EBSD results of Grain 3 and Grain 4 shown in Figure 3.

Therefore, it can be found that after cyclic heat treatment, the grain boundaries change from disordered large-angle grain boundaries to fine, coherent small-angle grain boundaries. The formation of refined grain with coherent boundaries is identified as two kinds of variant selection processes: (1) During the cooling process in the single-phase region, metastable γ structure can be promoted by Ta in TiAl-based alloys. Due to the tetragonality in the $L1_0$ γ metastable phase, the length in a direction is larger than the b and c directions. The (110) direction is not equivalent to the other two (101) directions; three possible (110) directions can be identified in the {111} habit plane (Figure 5a). Meanwhile, two stacking faults, ABCABC and ACBACB, are observed. Thereafter, there exist six possible orientation variants for the γ metastable phase that originated from one given α grain. Thereafter, the growth of subgrains in metastable γ is the variants selection process along {111}γ habit plane [13], that make the adjacent γ grain have 120° rotational, twin-related (pseudo-twin or true-twin) coherent interface; (2) On the other hand, during short time holding at single α phase region, due to one γ phase having four close packed planes labeled as BCD, ADC, ABD, and ABC followed by the Thopmpson tetrahedral model (Figure 5b), four possible α_s variants are confined to precipitate from the coherent γ metastable phase. Based on this, the 71° misorientation of adjacent α_s grain in Figure 4a demonstrates these two α_s variants originated from one γ grain, which have been observed to be $\left\{\bar{3}301\right\} < 11\bar{2}0 > \alpha_2$ twinning [23]. Thereafter, based on the EBSD and TEM results, two types of coherent grain boundaries can be identified, as illustrated in Figure 5c. For Type I coherent boundary, the crystal structures of $\gamma1$ and $\gamma2$ grains are identical, while α_{s1} and α_{s2} grains display as twins. For the Type II coherent boundary, $\gamma2$ and $\gamma3$ grains display a 120° rotational interface, while the crystal structures of α_{s2} and α_{s3} grains are identical.
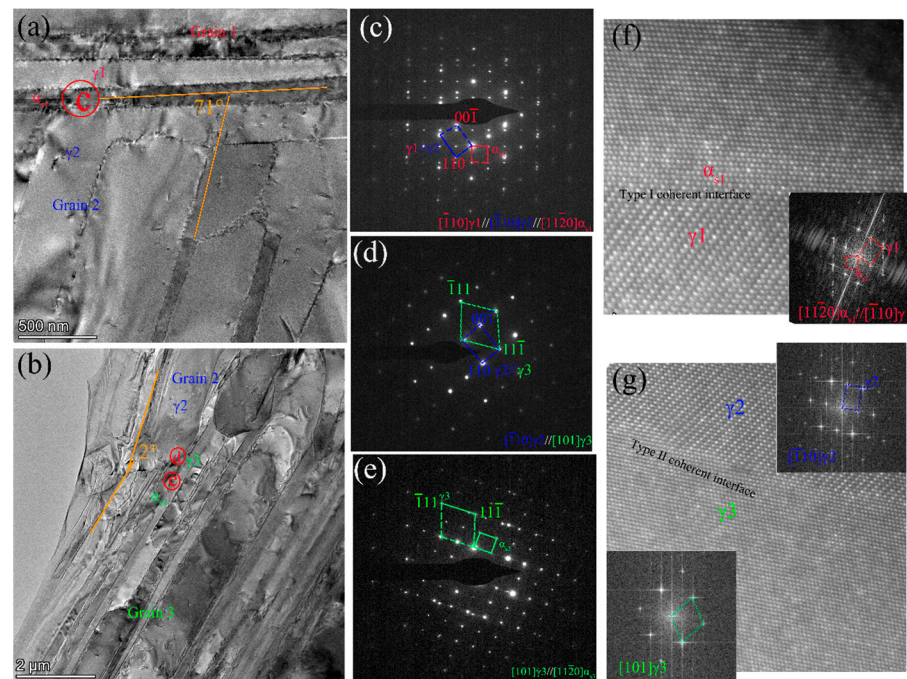
Figure 4. TEM images of coherent grain boundaries: (**a**) Type I coherent grain boundary and (**c**) corresponding SADPs in red cycle in (**a**); (**b**) Type II coherent boundary and (**d**,**e**) corresponding SADPs in red cycle in (**b**); (**f**,**g**) HAADF images of Type I and Type II coherent boundaries, respectively.
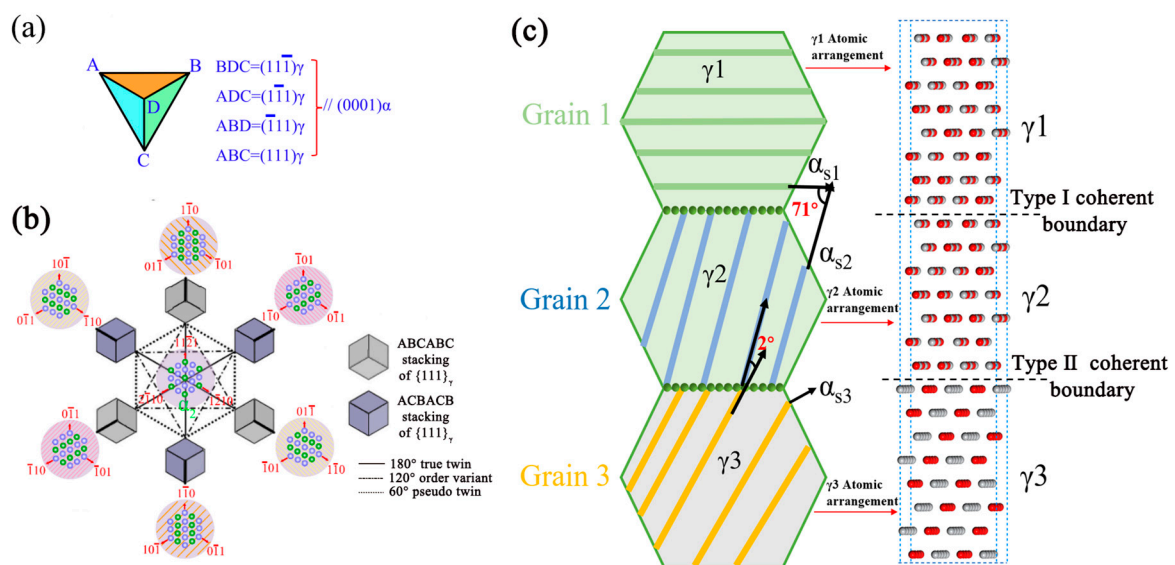

Figure 5. Schematic images: (**a**) Thopmpson tetrahedral model of the γ phase; (**b**) the six orientation variants of γ phase with the basal plane of a α grain; (**c**) the structure of coherent boundaries.

3.2. Isothermal Oxidation Behaviors

The original microstructures of both coarse FL (CFL) and fine FL (FFL) alloys are shown in Figure 1b,c, respectively. After being isothermally exposed at 1000 °C for 100 h, the mass gain of both CFL and FFL alloys is measured and summarized in Figure 6a. It is obvious that the mass gain increases significantly with the increase in exposure time. The details of the relationship between oxidation mass gain (ΔM) and oxidation time (*t*) can be calculated by the linear fitting equation in Equation (1):

$$(\Delta M)^n = kt \tag{1}$$

where k is the oxidation reaction rate constant ($mg^n/cm^{2n}\cdot h$) and n is the oxidation reaction exponent [10,24]. After fitting calculation, the values of n for CFL alloy and FFL alloy are 1.82 and 2.07, respectively. Compared with the CFL alloy, the FFL alloy has a higher n value, which indicates better oxidation resistance at 1000 °C. In general, the mass gain of the FFL alloy is 3.09 mg/cm^2, which is 31.6% lower than that of the CFL alloy (4.52 mg/cm^2). Under this condition, the oxidation rate constant of FFL alloy ($k = 0.0773$) is 46.7% lower than that of CFL alloy ($k = 0.1449$).
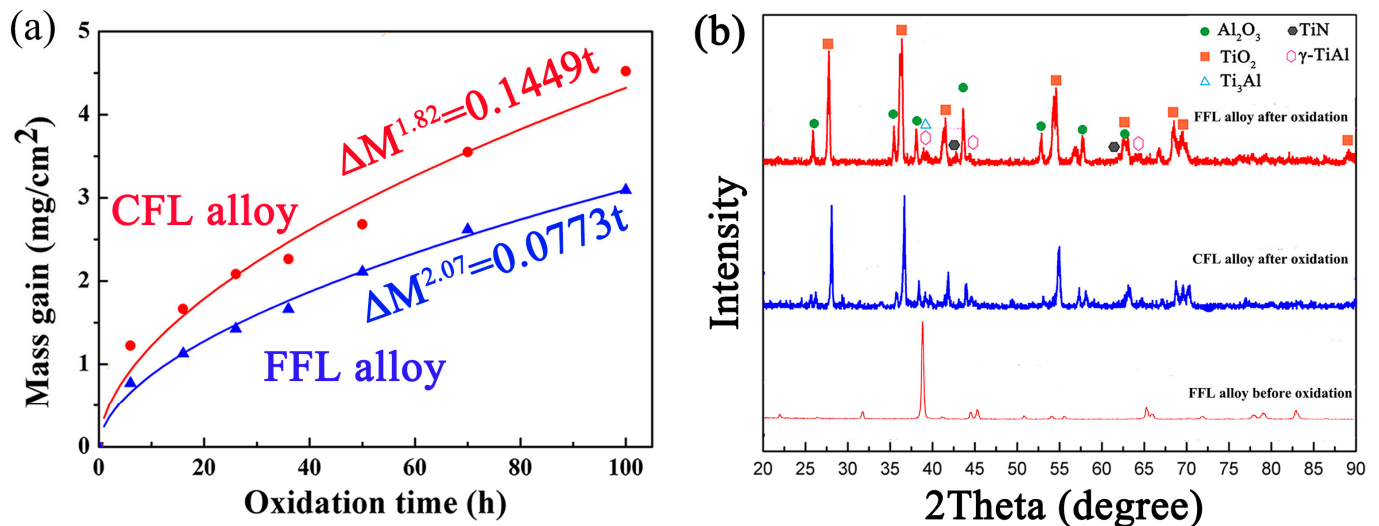

Figure 6. (**a**) Oxidation mass gain curve of CFL and FFL alloys at 1000 °C for 100 h; (**b**) corresponding XRD diffraction patterns.

Figure 6b illustrates the XRD diffraction patterns of FFL alloys before the oxidation process and CFL and FFL alloys after the oxidation process at 1000 °C for 100 h. It is clearly shown that the surface of both alloys is mainly composed of TiO_2 and Al_2O_3 particles. Furthermore, the peak intensity of TiO_2 increases while that of Al_2O_3 decreases in the FFL alloy compared with the CFL alloy, indicating that the oxidation surface of the FFL alloy is mainly composed of TiO_2. The weak diffraction peaks of TiN can also be identified by the XRD patterns. Nitrogen at high temperatures has a strong binding force with the Ti element; thus, TiN is identified after oxidation. Moreover, compared with other TiAl-based alloys conducted in previous studies [8,11,25–27], the FFL alloys possess the best oxidation resistance at 1000 °C for 100 h, which is even higher than the high Nb-containing TiAl-based alloys, attributed to the refinement of grain size (Figure 7).

*3.3. Microstructure of Surface and Cross-Section after Oxidation*

The surface morphology of CFL and FFL alloys after 100 h of oxidation is depicted in Figure 8. For CFL alloy, oxidation surface morphologies (Figure 8a) illustrate coarse and less dense non-uniform oxidation particles. The corresponding composition measured by EDS (Figure 8c,d, spot 1) shows the large particles containing 42% O and 23% Al should be Al_2O_3 particles. The small particles that gather together contain 29% O and 51% Ti (Figure 8c,d, spot 2) and should be TiO_2. This indicates that the surface is composed of large $TiO_2 + Al_2O_3$ particles. In contrast, the oxidation particles of the FFL alloy are more uniform and smaller (Figure 8b) compared with those of the CFL alloy. The EDS analysis reveals uniformly distributed small TiO_2 oxide particles on the surface, as shown in Figure 8e,f, spot 1, with a composition of 32% O and 5% Ti. The small Al_2O_3 particles containing 38% O and 29% Al (spot 2) distribute under the TiO_2 layer.
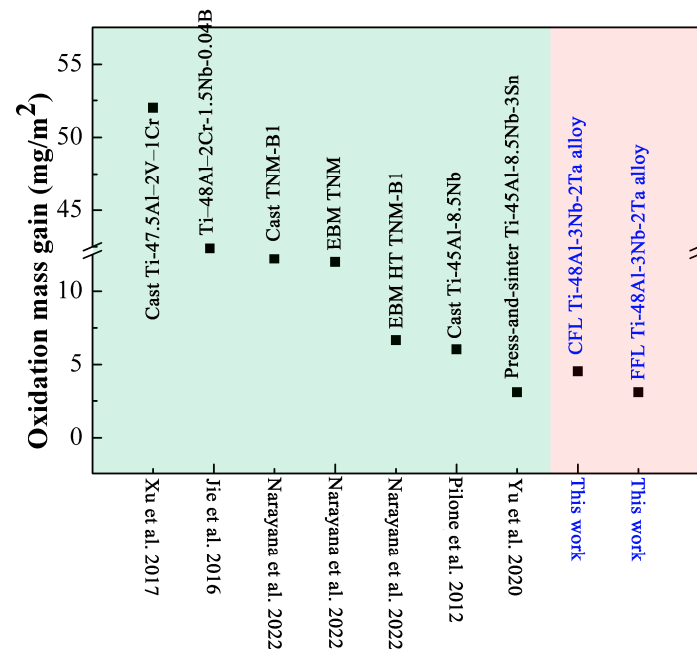
Figure 7. Oxidation resistance of CFL and FFL alloys at 1000 °C for 100 h compared with the data in literature (note: EBM: electron beam melting; HT: Heat treatment) [8,11,24–26].

The SEM images of oxide layers and their corresponding compositional maps in the cross-section are shown in Figure 9. For the CFL alloy (Figure 9a), layer I is identified as an $Al_2O_3 + TiO_2$ mixed layer, and the size of Al_2O_3 and TiO_2 particles is growing to be large for the high-temperature oxidation process. Meanwhile, the N element is enriched near the TiO_2 particles, which is confirmed to be TiN by XRD (Figure 6b). The mixed layer is then replaced by a continuous and protective Al_2O_3 layer (II). Layer III is a continuous layer of TiO_2, while layer IV represents another mixed $Al_2O_3 + TiO_2$ layer with solid solutions of Nb and Ta in TiO_2. Finally, the innermost layer V is identified as a mixed layer of TiN, Al_2O_3, and a discontinuous (Nb,Ta)-rich phase.
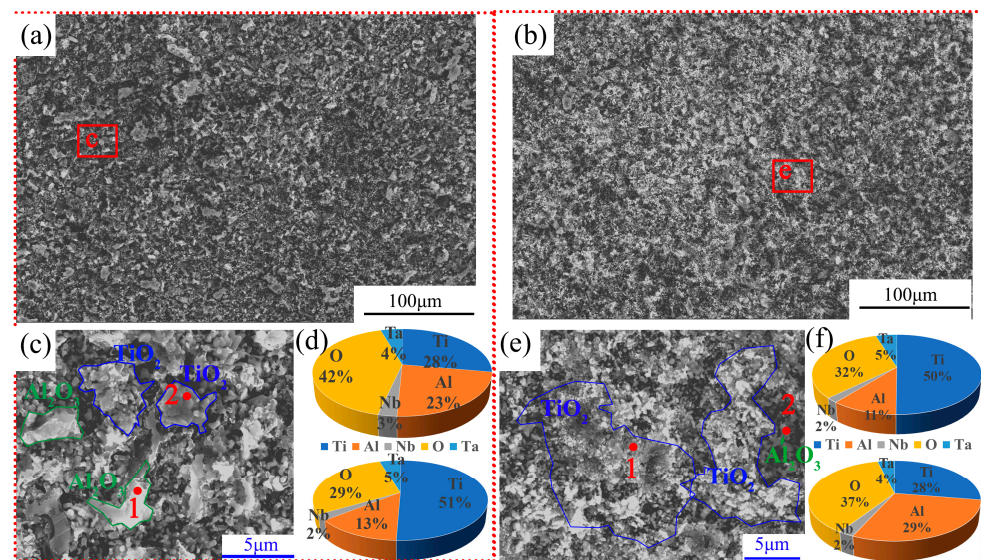
Figure 8. The surface morphology after oxidation of CFL alloy (**a**) and FFL alloy (**b**); (**c**,**d**) the enlarged view and corresponding composition marked in (**a**); (**e**,**f**) the enlarged view and corresponding composition marked in (**b**).
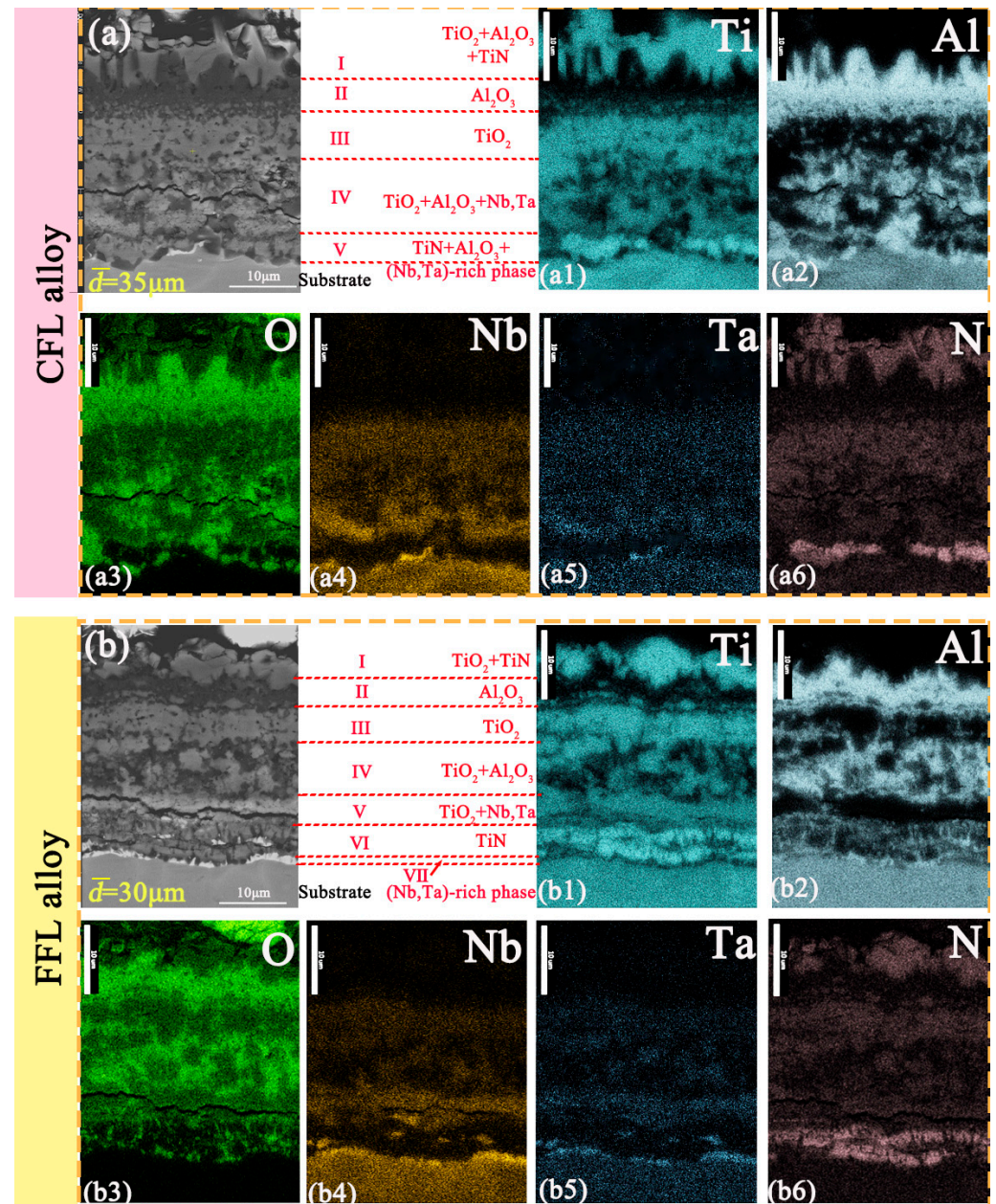
Figure 9. The cross-sectional morphologies of CFL and FFL alloys after oxidation at 1000 °C for 100 h: (**a**) SEM images of CFL alloy; (**a1**–**a6**) EDS composition mapping of rectangles marked in (**a**); (**b**) SEM images of FFL alloy; (**b1**–**b6**) EDS composition mapping of rectangles marked in (**b**).

For the FFL alloy (Figure 9b), however, layer I is identified as a single TiO_2 layer, which is also confirmed by XRD in Figure 6b and SEM in Figure 8b. Layer II consists of a continuous Al_2O_3 protective layer, followed by a continuous TiO_2 layer (III). Layer IV is a TiO_2 and Al_2O_3 mixed layer. It should be noted that layer V is a single and continuous TiO_2 layer again with solid solutions Nb and Ta. And layer VI is a continuous TiN layer with many fine-grained Al_2O_3 oxide pegs. The innermost layer VII is composed of a white and continuous (Nb,Ta)-rich layer about 1 μm.

Besides, a distinct feature is a Nb and Ta-depletion zone in the TiN layer, both in the CFL and FFL alloys, indicating the solubility of Nb and Ta in the TiN phase is limited. Furthermore, the thickness of the whole oxide film of CFL alloy and FFL alloy (Figure 9a,b) decreases from 35 μm to 30 μm.

In order to further illustrate the typical microstructure of the innermost oxide layer of both alloys, the transition zone morphology is illustrated in Figure 10, and the EDS composition content of points 1 to 7 is shown in Table 1. It can be clearly seen that for the CFL alloy in Figure 10a, the inner layer (IV) TiO_2 particles (point 1) with solid solution Nb and Ta are porous with white contrast and mixed with massive Al_2O_3 (point 2) with black contrast. For the innermost layer, TiN (point 3) is identified among the large Al_2O_3 peg and the discontinuous (Nb,Ta)-rich phase (Al $(Nb,Ta)_2$ (point 4)). It is worth noticing that this kind of discontinuous oxide film, especially the boundaries between the Al_2O_3 peg and the Al $(Nb,Ta)_2$ particle, cannot inhibit the oxygen from diffusing into the substrate; therefore, internal oxidation occurs during the whole oxidation process in the CFL alloy. In addition, for the FFL alloy (Figure 10b), a continuous TiO_2 layer (layer V) with solid solutions of Nb and Ta is observed (point 5). Especially, the content of Nb and Ta in TiO_2 of the point 1 and point 5 are 3.07Nb, 1.89Ta (CFL alloy), 8.47Nb, and 3.81Ta (FFL alloy), respectively, indicating more Nb and Ta can enrich the TiO_2 of the FFL alloy. A continuous TiN (VI, point 6) layer is identified, followed by the TiO_2 layer accompanied by fine-grained Al_2O_3 oxide pegs. The innermost layer VII is confirmed as continuous $Al(Nb,Ta)_2$ (point 7). Thereafter, continuous $(Ti, (Nb, Ta))O_2$, TiN, and $Al(Nb,Ta)_2$ multi-layers can provide good protection during oxidation.
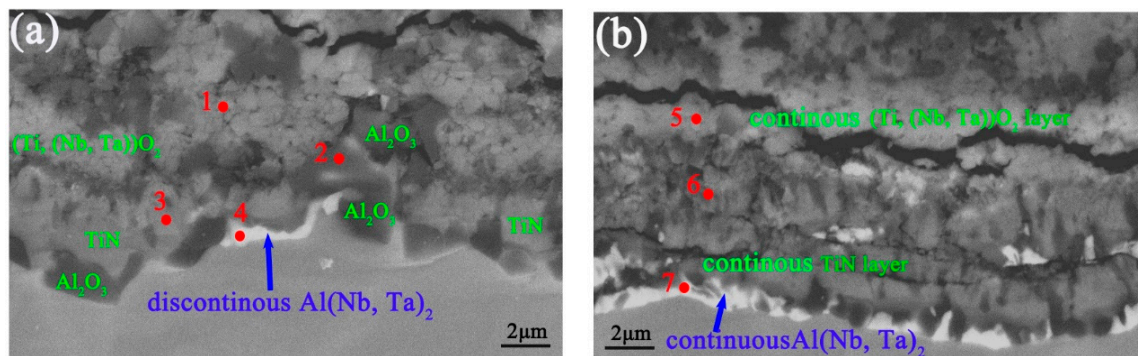
Figure 10. The transition zone morphology of (**a**) CFL alloy and (**b**) FFL alloy.

Table 1. The EDS composition results of sites from 1 to 7 are marked in Figure 10.

| Site	Element Composition (wt.%)						Corresponding Oxide
	Ti	Al	Nb	Ta	O	N	
1	47.66	10.52	3.07	1.89	33.27	3.59	TiO_2
2	19.21	41.17	2.27	1.21	36.14	0	Al_2O_3
3	38	14.6	1.4	1.2	34.6	10.2	TiN
4	21.35	42.22	18.13	7.06	4.97	6.27	$Al(Nb, Ta)_2$
5	50.34	13.23	8.47	3.81	20.92	3.23	TiO_2
6	50.07	27.32	1.67	1.3	8.55	11.09	TiN
7	24.76	44.6	15.28	6.35	5.63	3.38	$Al(Nb, Ta)_2$

4. Discussion

Figure 11 schematically describes the oxidation mechanisms of CFL and FFL alloys. The oxidation behavior is mainly controlled by element diffusion, which involves the outward diffusion of Ti, Al, Nb, and Ta ions and the inward diffusion of O and N ions, as indicated by the analysis of the oxidation mass gain curve (Figure 6a). Diffusion and oxidation occur at a given temperature T of 1000 °C. Oxygen diffusion is similar to the classical solid-state diffusion theory described by Equation (2):

$$D = D_0 \exp\left(-\frac{Q}{kT}\right) \tag{2}$$

where D_0 is the pre-exponential, Q is the activation energy, and k is the universal gas constant. The diffusion coefficients D in the grain area and the boundary area are different

due to the different values of Q. In the grain area with a coherent interface, the barrier over which atoms jump is larger than that in the boundary area. It has been certified that the D value in the boundary area is at least two orders higher than the grain area [18]. In other words, the diffusion at large-angle grain boundaries is much faster than the grain phase or the coherent interfaces.
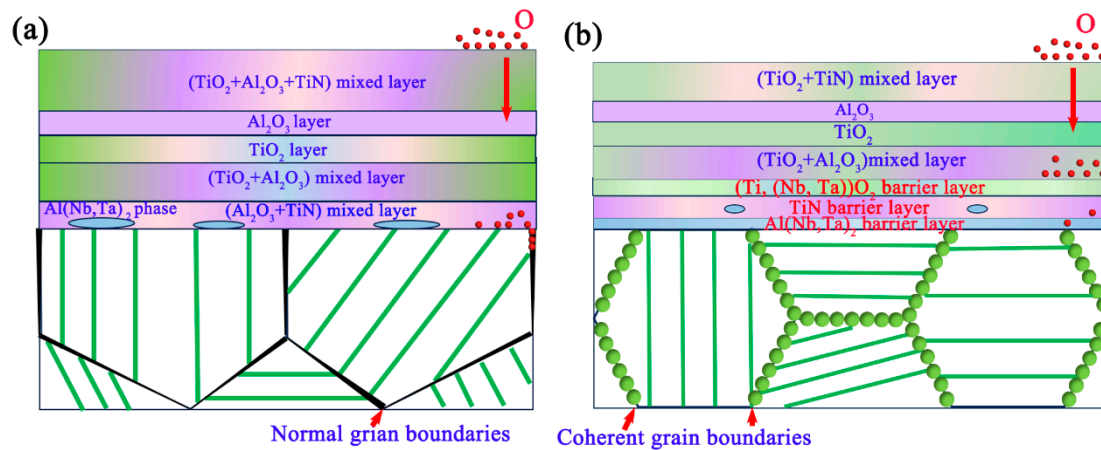
Figure 11. Schematic diagram of oxidation process of CFL alloy (**a**) and FFL alloy (**b**).

Based on this, although CFL alloys have a small amount of grain boundaries, they can provide the path for the diffusion of Ti, Nb, Ta, and Al ions to the outside and diffusion of O and N ions to the inside, resulting in large and less dense $TiO_2 + Al_2O_3$ mixed oxide particles at the outmost layer. With the consumption of Ti and Al, the Al_2O_3 layer, $Al_2O_3 + TiO_2$ mixed layer, TiO_2 layer, $Al_2O_3 + TiO_2$ mixed layer, and discontinuous TiO_2, TiN, and Al $(Nb,Ta)_2$ phases are formed in sequence. In this situation, the oxide films, especially the discontinuous innermost Al_2O_3 peg and Al $(Nb,Ta)_2$ particles, are not protective enough to inhibit the inward diffusion of O and N ions, which is also certified by other studies [10,28]. The study conducted by Gao et al. [29] also confirms that the discontinuous TiO_2, TiN, and Al $(Nb,Ta)_2$ phases next to the substrate are observed after oxidation for 200 h at 900 °C in the TiAl-1.5 Ta alloy with a coarse lamellae microstructure.

For the FFL alloy, due to the formation of different kinds of coherent grain boundaries, the diffusion velocity for O, N, Ti, and Al can be slowed down in contrast with the large-angle grain disorder grain boundaries. TiO_2, with more oxygen vacancies, grows faster than Al_2O_3 [18]. As a result, uniformly distributed small TiO_2 oxide particles form on the surface. Furthermore, Ti, Nb, and Ta have similar valence electronic structures and ionic radii for 0.64 Å of Nb^{5+}, 0.72 Å Ta^{5+}, and 0.605 Å of Ti^{4+} [30]. Ti, Nb, and Ta can mutually dissolve [31], resulting in Nb and Ta occupying the position of Ti to form the $(Ti, (Nb, Ta))O_2$ layer. Therefore, Nb and Ta can be distributed uniformly during the diffusion process instead of segregating at disordered grain boundaries, which can promote the formation of a continuous $(Ti, (Nb, Ta))O_2$ layer near the substrate.

While the concentration of O can be reduced by the continuous $(Ti, (Nb, Ta))O_2$ layer, nitrogen remains trapped in the innermost area. Due to the strong binding force with the Ti element, Equation (3) is activated to form a continuous TiN layer, as shown below:

$$Ti + [N] = TiN \tag{3}$$

where [N] represents atoms or ions initiating the dissolution and decomposition of nitrogen at high temperatures. Usually, TiN, which is selected as a wear-resistant coating, is an extremely hard ceramic material. The nano hardness and elastic modulus for TiN film are 20.50 GPa and 281.66 GPa, respectively [31], which can improve the wear, corrosion, and even oxidation properties of alloys because a continuous nitride layer can prevent fast internal oxidation [32].

Besides, the formation of TiN could consume the Ti element, and TiN has a low solubility for Nb and Ta (Figure 10 and Table 1) due to the strong Ti-N bond [33]. The reaction of $(Nb,Ta)O_2$ and Al at the film/substrate interface can be promoted to form the $Al(Nb,Ta)_2$ phase with fine-grained Al_2O_3 oxide pegs via Equation (4) [8].

$$11Al + 6(Nb,Ta)O_2 = 3Al(Nb,Ta)_2 + 4Al_2O_3 \qquad (4)$$
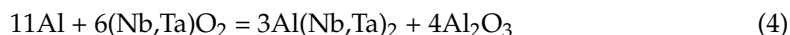
As a result, the innermost oxide films with continuous multi-layered (Ti, (Nb, Ta))O_2, TiN, and $Al(Nb,Ta)_2$ layers in FFL alloys are formed, which can greatly reduce the diffusion rate of oxygen and nitrogen. Evidently, the FFL alloys possess the best oxidation resistance at 1000 °C for 100 h, which is even higher than the high Nb-containing TiAl-based alloys, attributed to the refinement of grain size.

The improvement in oxidation resistance of the FFL TiAl alloy is mainly contributed by the following aspects: (1) the coherent boundaries have lower diffusion coefficients than the grain boundaries, which can slow down the diffusion of oxidation towards the substrate; (2) heavy elements such as Nb and Ta are uniformly distributed during the diffusion process instead of being segregated at disordered grain boundaries, which promotes the formation of a continuous (Ti, (Nb, Ta))O_2 layer; (3) the formation of a continuous TiN and $Al(Nb,Ta)_2$ layer can be induced by the (Ti, (Nb, Ta))O_2 layer, inhibiting O and N atom diffusion.

5. Conclusions

The refinement of TiAl-based alloys (CFL and FFL) prepared by cyclic heat treatment and their corresponding isothermal oxidation behavior were compared in detail. The grain refinement process and related oxidation mechanisms are revealed. The main results are as follows:

(1)   The CFL (~400 μm) TiAl alloy can be refined to 40 μm through metastable γ structures by cyclic heat treatment. After oxidation tests at 1000 °C for 100 h, the lowest mass gain is 3.09 mg/cm^2 of the FFL alloy, which is 31.6% lower than the CFL alloy.

(2)   Two kinds of variant selection processes: the coherent metastable γ variants of 120° rotational interface precipitated during the air-cooling process to form a Type II coherent boundary, as well as $α_s$ variants originated from one metastable γ variant during holding at the single α phase region process, could promote the formation of Type I coherent boundaries of FFL alloy.

(3)   Coherent grain boundaries can reduce oxidation diffusion toward the substrate. Additionally, heavy elements of Nb and Ta are uniformly distributed during the diffusion process instead of being segregated at disordered grain boundaries. This promotes the formation of a continuous protective barrier consisting of (Ti, (Nb, Ta))O_2, TiN, and $Al(Nb,Ta)_2$ layers.

References

1. Chen, G.; Peng, Y.; Zheng, G.; Qi, Z.; Wang, M.; Yu, H.; Dong, C.; Liu, C.T. Polysynthetic twinned TiAl single crystals for high temperature applications. *Nat. Mater.* **2016**, *14*, 876–881. [CrossRef] [PubMed]
2. Kim, J.Y.; Park, E.S.; Lee, T.; Ryu, S.; Kim, S.E.; Kim, S.W. Origin of enhanced room temperature ductility in TiAl alloys: Reducing activation difference of deformation mechanism of γ phase. *J. Alloys Compd.* **2022**, *899*, 163307. [CrossRef]
3. Fang, H.; Wang, S.; Chen, R.; Xu, Q.; Yan, Y.; Su, Y.; Guo, J. The effects of the formation of a multi-scale reinforcing phase on the microstructure evolution and mechanical properties of a Ti2AlC/TiAl alloy. *Nanoscale* **2021**, *13*, 12565. [CrossRef] [PubMed]
4. Sun, T.; Guo, Z.; Cao, J.; Liang, Y.; Lin, J. Isothermal oxidation behavior of high-Nb-containing TiAl alloys doped with W, B, Y, and C/Si. *Corros. Sci.* **2023**, *213*, 110980. [CrossRef]
5. Pflumm, R.; Donchev, A.; Mayer, S.; Clemens, H.; Schütze, M. High-temperature oxidation behavior of multi-phase Mo-containing γ-TiAl-based alloys. *Intermetallics* **2014**, *53*, 45–55. [CrossRef]
6. Mitoraj, M.; Godlewska, E.M. Oxidation of Ti-46Al-8Ta in air at 700 °C and 800 °C under thermal cycling conditions. *Intermetallics* **2013**, *34*, 112–121. [CrossRef]
7. Swadźba, R.; Marugib, K.; Pyclik, Ł. STEM investigations of γ-TiAl produced by additive manufacturing after isothermal oxidation. *Corros. Sci.* **2020**, *169*, 108617. [CrossRef]
8. Yu, P.; Xin, L.; Muhammad, D.H.; Yang, F.; Liu, C.; Li, Y.; Li, X.; Xu, W.; Qu, X.; Cao, P. Effect of Sn addition on the high-temperature oxidation behavior of high Nb-containing TiAl alloys. *Corros. Sci.* **2020**, *166*, 108449.
9. Tian, S.; He, A.; Liu, J.; Zhang, Y.; Yang, Y.; Zhang, Y.; Jiang, H. Oxidation resistance of TiAl alloy improved by hot-pack rolling and cyclic heat treatment. *Mater. Charact.* **2021**, *178*, 111196.
10. Liang, Z.; Xiao, S.; Yue, H.; Li, X.; Li, Q.; Zheng, Y.; Xu, L.; Xue, X.; Tian, J.; Chen, Y. Tailoring microstructure and improving oxidation resistance of an additively manufactured high Nb containing TiAl alloy via heat treatment. *Corros. Sci.* **2023**, *220*, 111287. [CrossRef]
11. Narayana, P.L.; Kima, J.H.; Yun, D.W.; Kim, S.E.; Reddy, N.S.; Yeom, J.T.; Seo, D.; Hong, J.K. High temperature isothermal oxidation behavior of electron beam melted multi-phase γ-TiAl alloy. *Intermetallics* **2022**, *141*, 107424. [CrossRef]
12. Garip, Y. Investigation of isothermal oxidation performance of TiAl alloys sintered by different processing methods. *Intermetallics* **2020**, *127*, 106985. [CrossRef]
13. Zhang, K.R.; Hu, R.; Lei, T.C.; Yang, J.R. Refinement of massive γ phase with enhanced properties in a Ta containing γ-TiAl-based alloys. *Scripta Mater.* **2019**, *172*, 113–118. [CrossRef]
14. Hu, R.; Wu, Y.; Yang, J.; Gao, Z.; Li, J. Phase transformation pathway and microstructural refinement by feathery transformation of Ru-containing γ-TiAl alloy. *J. Mater. Res. Technol.* **2022**, *18*, 5290–5300. [CrossRef]
15. Wei, D.X.; Koizumi, Y.; Nagasako, M.; Chiba, A. Refinement of lamellar structures in Ti-Al alloy. *Acta Mater.* **2017**, *125*, 81–97. [CrossRef]
16. Zhang, K.R.; Hu, R.; Li, J.; Yang, J.; Gao, Z. Grain refinement of 1 at.% Ta-containing cast TiAl-based alloy by cyclic air-cooling heat treatment. *Mater. Lett.* **2020**, *274*, 127940. [CrossRef]
17. Yim, S.; Bian, H.; Aoyagi, K.; Chiba, A. Effect of multi-stage heat treatment on mechanical properties and microstructure transformation of Ti–48Al–2Cr–2Nb alloy. *Mat. Sci. Eng. A* **2021**, *816*, 141321. [CrossRef]
18. Chepak-Gizbrekh, M.V.; Knyazeva, A.G. Oxidation of TiAl alloy by oxygen grain boundary diffusion. *Intermetallics* **2023**, *162*, 107993. [CrossRef]
19. Liu, Y.; Hu, R.; Kou, H.; Zhang, T.; Wang, J.; Li, J. A mixture of massive and feathery microstructures of Ti48Al2Cr2Nb alloy by high undercooled solidification. *Mater. Charact.* **2015**, *100*, 104–107. [CrossRef]
20. Dey, S.R.; Bouzy, E.; Hazotte, A. Features of feathery γ structure in a near-γ TiAl alloy. *Acta Mater.* **2008**, *56*, 2051–2062. [CrossRef]
21. Lapin, J.; Marek, K. Effect of continuous cooling on solid phase transformations in TiAl-based alloy during Jominy end-quench test. *J. Alloys Compd.* **2018**, *735*, 338–348. [CrossRef]
22. Saage, H.; Huang, A.J.; Hu, D.; Loretto, M.H.; Wu, X. Microstructures and tensile properties of massively transformed and aged Ti46Al8Nb and Ti46Al8Ta alloys. *Intermetallics* **2009**, *17*, 32–38. [CrossRef]
23. Gao, Z.; Hu, R.; Zou, H.; Li, J.; Zhou, M.; Luo, X. Metastable microstructure evolution and grain refinement in a Low-Ta containing γ-TiAl alloy through heat treatment. *J. Mater. Res. Technol.* **2024**, *29*, 3642–3655. [CrossRef]
24. Xu, Y.X.; Lu, J.T.; Yang, X.W.; Yan, J.B.; Li, W.Y. Effect and role of alloyed Nb on the air oxidation behaviour of Ni-Cr-Fe alloys at 1000 °C. *Corros. Sci.* **2017**, *127*, 10–20. [CrossRef]
25. Jie, L.; Xiangyi, X. Isothermal oxidation behavior of TiAl-Nb-W-B-Y alloys with different lamellar colony sizes. *Rare Met. Mater. Eng.* **2016**, *45*, 1695–1699. [CrossRef]
26. Pilone, D.; Felli, F. Isothermal oxidation behaviour of TiAl-Cr-Nb-B alloys produced by induction melting. *Intermetallics* **2012**, *26*, 36–39. [CrossRef]
27. Gui, W.; Liang, Y.; Qin, J.; Wang, Y.; Lin, J. Fluorine Effect for Improving Oxidation Resistance of Ti-45Al-8.5Nb Alloy at 1000 °C. *Materials* **2022**, *15*, 2767. [CrossRef]
28. Dadéa, M.; Esin, V.A.; Nazéa, L.; Sallot, P. Short- and long-term oxidation behaviour of an advanced Ti2AlNb alloy. *Corros. Sci.* **2019**, *148*, 379–387. [CrossRef]
29. Gao, Z.; Hu, R.; Zou, H.; Zhou, M.; Luo, X. Insight into the Ta alloying effects on the oxidation behavior and mechanism of cast TiAl alloy. *Mater. Design* **2024**, *241*, 112941. [CrossRef]

30. Zatsepin, D.A.; Boukhvalov, D.W.; Kurmaev, E.Z.; Zhidkov, I.S.; Kim, S.S.; Cui, L.; Gavrilov, N.V.; Cholakh, S.O. XPS and DFT study of Sn incorporation into ZnO and TiO$_2$ host matrices by pulsed ion implantation. *Phys. Status Solidi* **2015**, *252*, 1890–1896. [CrossRef]

31. Dai, J.J.; Zhu, J.Y.; Chen, C.Z.; Weng, F. High temperature oxidation behavior and research status of modifications on improving high temperature oxidation resistance of titanium alloys and titanium aluminides: A review. *J. Alloys Compd.* **2016**, *685*, 784–798. [CrossRef]

32. Quadakkers, W.J.; Schaaf, P.; Zheng, N.; Gil, A.; Wallura, E. Beneficial and detrimental effects of nitrogen on the oxidation behaviour of TiAl-based intermetallics. *Mater. Corros.* **1997**, *48*, 28–34.

33. Wang, S.; Zhang, Y.; Qin, Y.; Lu, J.; Liu, W. Improvement of TiN coating on comprehensive performance of NiTi alloy braided vascular stent. *Ceram. Int.* **2023**, *49*, 13405–13413. [CrossRef]